JGR Space Physics

RESEARCH ARTICLE
10.1029/2021JA029117

Geospace Plume and Its Impact on Dayside Magnetopause Reconnection Rate

Ying Zou[1], Brian M. Walsh[2], Xueling Shi[3,4], Larry Lyons[5], Jiang Liu[5,6], Vassilis Angelopoulos[6], John M. Ruohoniemi[3], Anthea J. Coster[7], and Michael G. Henderson[8]

[1]Department of Space Science, University of Alabama in Huntsville, Huntsville, AL, USA, [2]Department of Mechanical Engineering and Center for Space Physics, Boston University, Boston, MA, USA, [3]The Bradley Department of Electrical and Computer Engineering, Virginia Tech, Blacksburg, VA, USA, [4]High Altitude Observatory, National Center for Atmospheric Research, Boulder, CO, USA, [5]Department of Atmospheric and Oceanic Sciences, University of California, Los Angeles, CA, USA, [6]Department of Earth, Planetary and Space Sciences, University of California, Los Angeles, CA, USA, [7]Massachusetts Institute of Technology Haystack Observatory, Westford, MA, USA, [8]Los Alamos National Laboratory, Los Alamos, NM, USA

Key Points:

- We strategically coordinate measurements made by THEMIS and Los Alamos National Laboratory spacecraft, GPS network, and SuperDARN to investigate geospace plumes
- Plumes decrease the local reconnection rate at the plume longitude and increase the reconnection rate in regions adjacent to the plume
- When the solar wind is stable, the global reconnection remains unchanged in presence of plumes, supporting a global-control theory

Correspondence to:
Y. Zou,
yz0025@uah.edu

Citation:
Zou, Y., Walsh, B. M., Shi, X., Lyons, L., Liu, J., Angelopoulos, V., et al. (2021). Geospace plume and its impact on dayside magnetopause reconnection rate. *Journal of Geophysical Research: Space Physics*, *126*, e2021JA029117. https://doi.org/10.1029/2021JA029117

Received 8 JAN 2021
Accepted 20 MAY 2021

Abstract

The role a geospace plume in influencing the efficiency of magnetopause reconnection is an open question with two contrasting theories being debated. A local-control theory suggests that a plume decreases both local and global reconnection rates, whereas a global-control theory argues that the global reconnection rate is controlled by the solar wind rather than local physics. Observationally, limited numbers of point measurements from spacecraft cannot reveal whether a local change affects the global reconnection. A distributed observatory is hence needed to assess the validity of the two theories. We use THEMIS and Los Alamos National Laboratory spacecraft to identify the occurrence of a geospace plume and its contact with the magnetopause. Global evolution and morphology of the plume is traced using GPS measurements. SuperDARN is then used to monitor the distribution and the strength of dayside reconnection. Two storm-time geospace plume events are examined and show that as the plume contacts the magnetopause, the efficiency of reconnection decreases at the contact longitude. The amount of local decrease is 81% and 68% for the two events, and both values are consistent with the mass loading effect of the plume if the plume's atomic mass is ~4 amu. Reconnection in the surrounding is enhanced, and when the solar wind driving is stable, little variation is seen in the cross polar cap potential. This study illuminates a pathway to resolve the role of cold dense plasma on solar wind-magnetosphere coupling, and the observations suggest that plumes redistribute magnetopause reconnection activity without changing the global strength substantially.

Plain Language Summary

A variety of magnetospheric plasma populations exist at the interface where the solar wind encounters the magnetosphere, and they can impact the efficiency of the energy transfer from the solar wind to the magnetosphere. One population of particular interest is geospace plumes, which are plumes of cold dense plasma of ionospheric origin drifting sunward toward the magnetopause during enhanced geomagnetic activity. Plumes often have a density much higher than the other magnetospheric populations and can therefore mass load the dayside magnetopause slowing down magnetic reconnection. However, whether reconnection is slowed at a local or global scale is under debate. Observationally, point measurements from spacecraft cannot reveal whether a local change affects the global reconnection and a distributed observatory is hence needed. In this study we strategically coordinate measurements made by THEMIS and Los Alamos National Laboratory spacecraft, GPS network, and SuperDARN to investigate the effect of plumes on reconnection. Our results suggest that plumes decrease the local reconnection rate at the plume longitude and increase the reconnection rate in regions adjacent to the plume. When the solar wind is stable, the global reconnection remains unchanged. Such observations illuminate a pathway to resolve the role of cold dense plasma on solar wind-magnetosphere coupling.

1. Introduction

The concept of geospace plume is introduced to describe a system-wide redistribution of cold (<several eV) plasma of ionospheric origin in the ionosphere, plasmasphere, and magnetosphere, which frequently occurs during geomagnetic disturbances (Foster et al., 2020). In the plasmasphere, the geospace plume manifests as a plasmaspheric (drainage) plume (Ober et al., 1997), or a plasmaspheric tail as named in early literature (e.g., Chappell, 1974; Maynard & Chen, 1975). When the interplanetary magnetic field (IMF) turns southward, the plasmapause, that is, formed by the combination of the corotational and solar wind-driven convection electric fields moves inward, causing the outer layers of the plasmasphere to be peeled away. This forms a sunward bulge and a long tail toward the dayside magnetosphere (A. J. Chen & Grebowsky, 1978; A. J. Chen & Wolf, 1972; Lemaire, 2000; Nishida, 1966). Plasmaspheric plumes play important roles in the magnetosphere, such as wave generation and wave–particle interactions (e.g., L. Chen et al., 2012; Halford et al., 2015; Summers et al., 2008), particle precipitation (Spasojevic & Fuselier, 2009; Yuan et al., 2011, 2013), and local-time asymmetries in ULF wave field-line resonance signatures (e.g., Archer et al., 2015; Ellington et al., 2016). Plasmaspheric plumes can also extend all the way to the dayside magnetopause, where they interact with the dayside reconnection site. In fact, plasmaspheric plumes are present for 10%–20% of the time at the magnetopause (André & Cully, 2012; Darrouzet et al., 2008; Lee et al., 2016; Walsh et al., 2013). How they impact the dayside magnetopause reconnection rate is the subject of this paper.

Two contrasting theories have been proposed to predict how plasmaspheric plumes impact the dayside magnetopause reconnection. A local-control theory (Borovsky et al., 2008, 2013) suggests that the plume decreases both local and global reconnection rates. In this theory, the dayside reconnection rate is determined entirely by four local plasma parameters: B_S (the magnetic field strength in the magnetosheath), B_M (the magnetic field strength in the magnetosphere), ρ_S (the plasma mass density in the magnetosheath), and ρ_M (the plasma mass density in the magnetosphere). Such a dependence is consistent with the formula proposed by Cassak and Shay (2007). Reconnection does not significantly modify these local plasma parameters, nor does it significantly alter the flow pattern of the magnetosheath, meaning that plasma would not pileup to change the local parameters to adjust the reconnection rate. As a result, the reconnection rate should decrease at regions where the plume interacts with reconnection owing to plume's high mass density, while it remains unchanged away from the plume. The integrated reconnection rate decreases.

On the other hand, a global-control theory argues that the global reconnection rate is controlled by the solar wind rather than local physics, and hence is not affected by the presence of plasmaspheric plumes (Lopez, 2016; Lopez et al., 2010). Specifically, Lopez et al. (2010) suggests that the fraction of the solar wind potential across the magnetosphere that is applied to the dayside merging region depends on how plasma flows are diverted away from the merging regions by forces in the magnetosheath. For high magnetosonic Mach numbers (weak and moderate IMF with $|B| < 15$ nT), the force balance is dominated by the pressure gradient force, and the flow pattern is controlled by the solar wind density, velocity, and temperature, and the ionospheric conductivity. For low Mach numbers, the force balance is dominated by the $J \times B$ force and the flow pattern additionally depends on the IMF. In either case, plasmaspheric plumes do not affect the global force balance in the magnetosheath. Therefore, although the plume decreases the local merging rate, the rate increases away from the plume so that the integrated rate remains unaltered.

Numerical simulations can investigate the local and integrated reconnection rates, as well as forces in the sheath, and can hence assess which theory better describes the impact of plasmaspheric plumes. MHD simulations conducted by Zhang et al. (2016, 2017) and Ouellette et al. (2016) indicate a mixed-control theory. It is found that a small amount of mass loading at the dayside magnetopause only redistributes local reconnection rate without a significant change in the integrated reconnection rate, whereas a large amount of mass loading reduces both local and integrated reconnection rates. The transition from global- to local-control-dominated regimes depends on (at least) three aspects of plasmaspheric plumes: density, location, and extent. In the specific simulation setup of Zhang et al. (2017), the global (local) control theory is valid when the mass density at the magnetopause inflow region is <8 amu/cm^3 (>16 amu/cm^3).

Both the developing theories and simulations are currently in need of experimental verification. However, in situ satellite measurements alone have limited capabilities because they can only provide a local measure

of reconnection properties in a snapshot of time. Nevertheless, Su et al. (2000) identified plasmaspheric material in the reconnection jets, suggesting that plasmaspheric plumes have participated in dayside reconnection. When plumes are present, Borovsky and Denton (2006) found that the geomagnetic indices become less strong than when plumes are absent for the same solar wind driving conditions. Walsh, Foster, et al. (2014) and Walsh, Phan, et al. (2014) showed that the reconnection jet speed, and possibly the reconnection rate, was lower, and that the location of the jet was primarily on field lines with magnetosheath orientation. Wang et al. (2015) computed the reconnection rate, but did not observe substantial reduction in the rate, probably because the plasma density of the plumes in their events was small. Lee et al. (2014) reported one case where the plume ions did not enter the reconnection diffusion region but flew directly into the reconnection outflow. In this case, the plume had limited impact on the reconnection rate.

To resolve the impact of plasmaspheric plumes, temporally continuous and spatially wide observations are necessary, as they provide useful information on what happens before and during the plume's encounter with the magnetopause, as well as what happens within and outside the encounter region. Fortunately, the fact that plasmaspheric plumes are one facet of a system-wide geospace plume phenomenon allows the utilization of a distributed network. GPS total electron content (TEC) measurements, for example, can identify and track storm enhanced density (SED) (Foster, 1993), which is the ionospheric element of the geospace plume. SED is a longitudinally extended and latitudinally narrow structure of elevated TEC that is often observed at the dusk sector and during the early stages of storms. It occurs near the equatorward edge of the midlatitude ionospheric trough, and convects sunward and poleward. SED is interpreted to result from the erosion of plasmas from the lower-latitude ionosphere by the electric field associated with sub-auroral polarization stream (SAPS) (Foster et al., 2007), which is the same electric field that erodes the outer plasmasphere. A number of studies have reported the connection between SED and plasmaspheric plumes (Foster et al., 2002, 2004, 2014, 2020; Walsh, Foster, et al., 2014; Yizengaw et al., 2006), implying that the connection may be a common feature (see the review by Moldwin et al., 2016).

The spatial-temporal evolution of dayside reconnection can be tracked remotely by radars including the SuperDARN radar network. One of the ionospheric signatures of reconnection is fast plasma flows moving anti-sunward across the ionospheric projection of the reconnection separatrix that separates the open and closed magnetic field lines, that is, the open-closed field line boundary (OCB) (Southwood, 1985). The OCB appears as a distinct boundary in the SuperDARN spectral width data, where low spectral width values are observed equatorward of the boundary, and high, but variable spectral width values poleward of the boundary (Chisham & Freeman, 2003, 2004; Chisham, Freeman, & Sotirelis, 2004; Chisham, Freeman, Lam, et al., 2005; Chisham, Freeman, Sotirelis, & Greenwald, 2005; Chisham, Freeman, Sotirelis, Greenwald, Lester, & Villain, 2005). The reconnection rate can then be estimated by measuring the magnetic flux transfer across the OCB in the frame of the OCB (Baker et al., 1997; Chisham et al., 2008; Chisham, Freeman, Coleman, et al., 2004; de la Beaujardiere et al., 1991; Freeman et al., 2007; Hubert et al., 2006; Pinnock et al., 1999, 2003; Zou et al., 2019). Its value in the ionosphere is typically a few tens of mV/m, which often corresponds to ~1 mV/m at the equatorial region of the magnetosphere.

Using the techniques above, we investigate the effect of geospace plumes on dayside reconnection by using coordinated observations of in situ and remote observations. We use THEMIS and Los Alamos National Laboratory (LANL) spacecraft to identify the occurrence of a geospace plume and its contact with the magnetopause. Global evolution and morphology of the plume is traced using GPS measurements. SuperDARN is then used to monitor the distribution and the strength of dayside reconnection. We describe our methodology in Section 2, present two geospace plume events in Section 3, and discuss the observations in the context of the local- and global-control theory in Section 4. Section 5 provides the conclusion of the work.

2. Methodology

THEMIS measurements are used to identify plumes that extend to the dayside magnetopause. The magnetopause is identified by a reversal of the B_z magnetic field from the fluxgate magnetometer (Auster et al., 2009) and/or a change in the ion energy spectra from the Electrostatic Analyzer (ESA) (McFadden, Carlson, Larson, Ludlam, et al., 2009). Plasma measurements just inside the magnetopause are inspected to discern the occurrence of plasmaspheric plume material. Although the cold plasmaspheric plasma is

normally below the energy threshold of ESA (~8 eV), at the magnetopause, the ions can be kinetically accelerated by large convection speeds such as those associated with magnetopause motion and/or magnetopause reconnection and become visible. They appear as a narrow spectral peak in the energy spectrograms, with the peak located at an energy corresponding to the plasma bulk velocity (McFadden, Carlson, Larson, Bonnell, et al., 2009). In addition, the density of the cold plasmaspheric electrons can be inferred from the spacecraft potential measured by EFI (Bonnell et al., 2008). Using these tools, we identify plumes by selecting ESA ion energy spectrograms that show a narrow spectral peak at the plasma bulk velocity and the spacecraft potential that corresponds to an electron density >10 cm^{-3}. The density threshold of 10 cm^{-3} is higher than those used by Walsh et al. (2013) and André and Cully (2012), but is the same as Darrouzet et al. (2008), suggesting that our studied plumes are comparatively dense.

Although we do not explicitly distinguish plumes from the warm plasma cloak (Chappell et al., 2008), cloaks are generally not expected to exhibit a narrow peak in the ion energy spectrograms because its typical temperature is ~10 eV to several keV, which is comparable or larger than the kinetic energy at the plasma bulk velocity. Existing cloak observations (e.g., Fuselier et al., 2016; Lee et al., 2016) support this expectation.

The presence/absence of plumes seen by THEMIS is validated by measurements from the Magnetospheric Plasma Analyzer (MPA) instruments on board the LANL geosynchronous satellites when calibrated data are available. Since MPAs typically float at a potential that is slightly negative with respect to the ambient plasma, all positively charged ions are detected by MPA (Bame et al., 1993; McComas et al., 1993; Thomsen et al., 1999). MPA has an energy range 1 eV–40 keV, and we identify plumes using the number density of cold plasmaspheric ions measured by the instrument. According to Sheeley et al. (2001), the plasmasphere is expected to have a density at geosynchronous orbits >10 cm^{-3}.

On a broader scale, GPS TEC measurements are used to identify and trace SED (Coster & Skone, 2009; Coster et al., 2003). TEC is calculated using phase and code delays of satellite signals received by dual-frequency ground receivers, and we use the global maps of GPS TEC from the Madrigal database maintained by Massachusetts Institute of Technology, Haystack Observatory (Rideout & Coster. 2006). By default, the data are binned into 1° × 1° cells at 5 min cadence, and we additionally apply a 3° × 3° median filter in space. One TEC unit (TECu) is given as 10^{16} el/m^2 and represents the total number of electrons contained in a column extending upward from the Earth's surface through the ionosphere with a cross sectional area of 1 m^2. Although TEC is an integral characteristic (electron content from the satellite to the ground), it is often used to characterize the state of the *F* region of the ionosphere because this region is the main contributor to the electron content. We visually select SED that extends into the OCB (identified through the SuperDARN data set) and occurs close to the footprints of THEMIS spacecraft. With the latter requirement, we can examine whether SED is located on the same closed magnetic field lines with the plasmaspheric plumes.

As suggested by Maruyama et al. (2020), the mechanism that physically links the plasmaspheric plume and SED is the enhanced duskside convection electric field, and the existence of such an electric field is examined using DMSP measurements. Specifically, the ion drift meter onboard the DMSP satellite measures the ion horizontal drift velocity component perpendicular to the satellite trajectory, and the electron and ion spectrometer (SSJ/4) measures particle fluxes of precipitating electrons and ions with energies from 30 eV to 30 keV every second. The existence of an electric field equatorward of the auroral precipitation, that is, SAPS, implies a connection in the cold plasma motion between the ionosphere and plasmasphere through $E \times B$ drift, and hence establishes a physical connection between the spatially collocated SED and the plasmaspheric plume.

The impact of SED on dayside magnetopause reconnection is remotely sensed by SuperDARN that measures the ionospheric convection. We look for fast anti-sunward flows moving across the OCB as the ionospheric counterpart of magnetopause reconnection. The OCB appears as a distinct boundary in the spectral width data. Statistically a spectral width boundary of 150 m/s serves as a good proxy for OCB (e.g., Baker et al., 1995, 1997; Chisham & Freeman, 2003) but the threshold can vary in individual events. The flow velocities are taken both from line-of-sight (LOS) measurements from individual radars, and global convection maps obtained through the spherical harmonic fit (Ruohoniemi & Baker, 1998). The velocities in the convection maps are more trustworthy at regions with dense backscatter echoes than those without, and therefore we mainly focus on the former. The global convection maps also provide cross polar cap

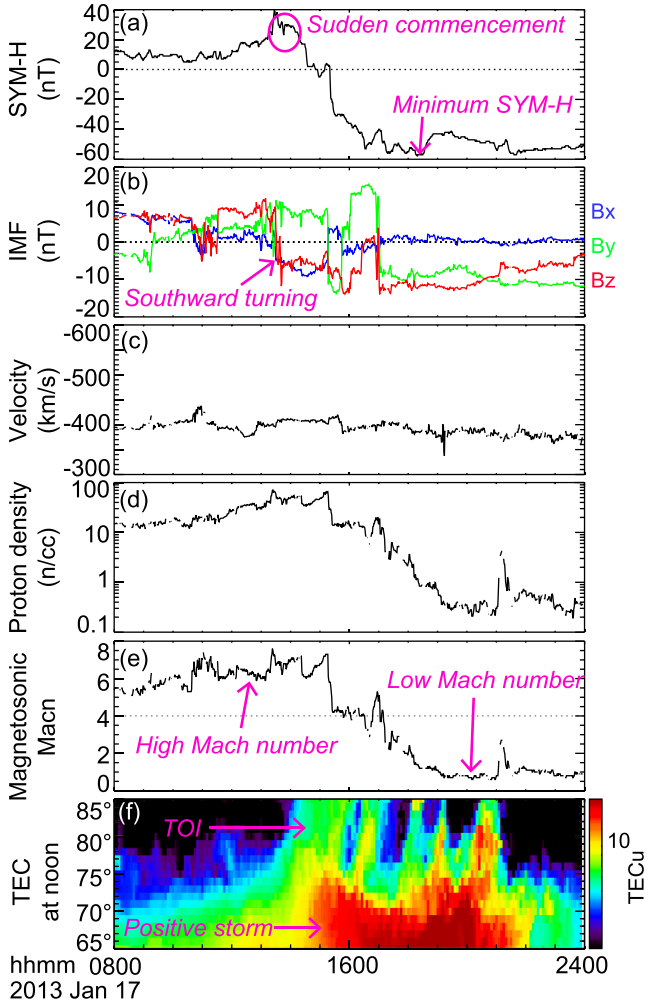

Figure 1. Overview of the geospace plume event on January 17, 2013. From top to bottom (a–f) shows the SYM-H index, interplanetary magnetic field in GSM coordinates, solar wind velocity component along GSM X, solar wind proton density, magnetosonic Mach number, and total electron content (TEC) at 10–14 h MLT. TOI, tongue of ionization.

potential (CPCP), which we use as a proxy of the global reconnection rate. The local reconnection rate is estimated by measuring the magnetic flux transfer across the OCB in the frame of the OCB and hence include the contribution from the motion of the plasma and the OCB.

We present two geospace plumes events with coordinated space-ground observations. One event occurred on January 17, 2013, and is the same event reported by Walsh, Foster, et al. (2014), where the authors found that local magnetopause reconnection was affected by a plume. However, Walsh, Foster, et al. (2014) did not provide measurements to quantify the plume's effect on the local and global reconnection rate, and we therefore revisit this event by including SuperDARN measurements to track the spatial-temporal evolution of reconnection. We find that that as the plume contacted the magnetopause, the reconnection rate decreased at the contact longitude, whereas the rate in the surrounding region increased. The second event occurred on October 11, 2010. This event has similar coordinated space-ground observations to the first event and was associated with prolonged steady IMF driving before and after a plume arrived at the magnetopause. The steady IMF provides an excellent opportunity to assess the global and local control theories, since the former predicts the global reconnection rate to remain unchanged, whereas the latter predicts a change due to plumes.

3. Observations

3.1. Geospace Plume on January 17, 2013

3.1.1. Occurrence of SED and Plasmaspheric Plume

As an overview of the event, the top four panels of Figure 1 present (from top to bottom) the SYM-H index, IMF, the solar wind velocity, number density, and magnetosonic Mach number on January 17, 2013 from OMNI data set. The SYM-H index showed a brief increase during ~1320–1420 UT (hhmm), signifying the sudden commencement phase of the storm, and then decreased and reached a minimum value of −58 nT at 1819 UT. This minimum value suggests that the storm was moderate in intensity. The storm persisted for ~3 days before returning to a quiet geomagnetic state, but the interval presented here was associated with a stronger southward IMF than the rest of the time, and hence a stronger convection inside the magnetosphere. The IMF was initially northward then turned southward sharply at ~1330 UT. It stayed mostly southward until the end of the interval of our interest (except for a brief period during 1630–1700 UT). The solar wind velocity was steady and stayed at ~400 km/s. The solar wind density showed an increase at ~1320 UT, simultaneously with the storm sudden commencement. The magnetosonic Mach number was high (>4) before 1700 UT, but then dropped toward one due to the combination of the large IMF and small solar wind density. The low Mach number implies that the global force balance that controls the pattern of the magnetosheath flow is dominated by the $J \times B$ force (Lopez et al., 2010), and that the pressure balance across the magnetopause is primarily contributed by magnetic pressure rather than plasma pressure on the magnetosheath side (Lopez & Gonzalez, 2017).

The bottom panel of Figure 1 presents the latitudinal distribution of TEC averaged over 1000–1400 MLT (±2 h from the magnetic noon). Following the storm commencement, positive storm effects appeared at middle latitudes and extended up to ~74° MLAT (poleward of 74° MLAT was the polar cap). Positive storm effects refer to a large increase in ionosphere F2 region electron density that occurs in the early phase of geomagnetic storms and frequently at middle latitudes in the afternoon to dusk sector (e.g., Buonsanto, 1995a, 1995b; Mendillo et al., 1972; Papagiannis et al., 1971). Various mechanisms have been proposed to explain the cause of this effect, including equatorward neutral winds, neutral composition changes (O/N_2

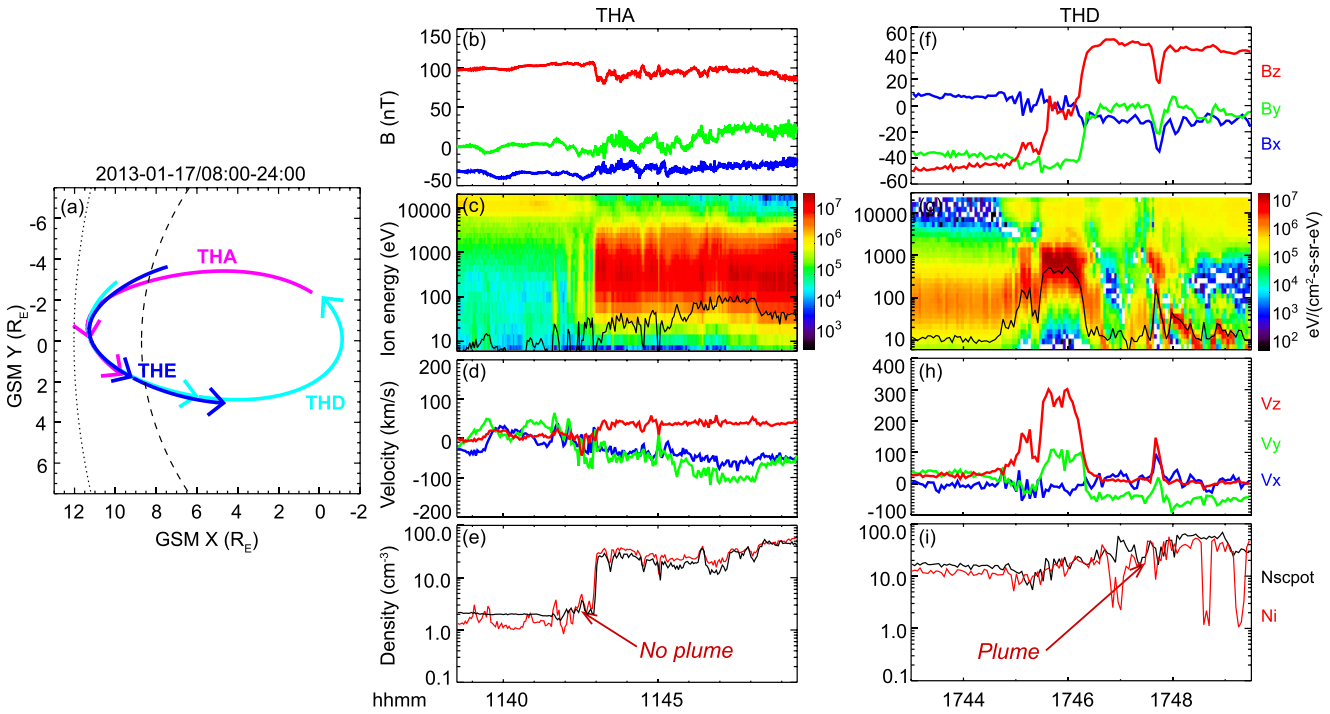

Figure 2. (a) THA, THD, and THE locations during 08–24 UT on January 17, 2013 projected to the GSM X-Y plane. The inner curve marks the magnetopause and the outer curve marks the bow shock. (b–e) THA measured magnetic field, ion energy spectrum, ion velocity, and ion density. The ion measurements were taken from ground Electrostatic Analyzer (ESA) moments. In addition to the ion density (red curve in Figure 2e), also shown is the plasma density inferred from spacecraft potential (black curve). Proton kinetic energy corresponding to the measured bulk flow velocity is indicated as black line in Panel (c). (f–i) Similar to Figures 2b–2e but showing measurements made by THD.

increases), penetration and disturbance dynamo electric fields, downward plasma flux from the plasmasphere, traveling atmospheric disturbances, and auroral particle precipitation (e.g., Buonsanto, 1999; Burns et al., 2007; Danilov, 2013; Mendillo, 2006; Prölss, 1995; Richmond & Lu, 2000). The enhanced electron density associated with the positive storm effects serves as an important plasma source of SED: when the increased electron density overlaps with equatorward edge of the two-cell plasma convection, the sunward convection electric field picks up the plasma and carries it toward local noon, forming SED. Two-dimensional maps of SED are presented in Figure 3, and in Figure 1f we can identify SED during periods when they extended into the polar cap. When SED are transported across the cusp into the polar cap, they form the tongue of ionization (TOI) and/or polar cap patches. In Figure 1f, TOI/patches appear as features extending from the midlatitude density enhancement and moving into the otherwise low-density polar cap region, as seen during 1400–2100 UT soon after the commencement of the storm.

Figure 2a shows the orbits of THEMIS spacecraft in GSM X-Y plane on this day. THA, THD, and THE had an apogee near local noon and passed the magnetopause on the duskside on the inbound leg of their orbits. Figures 2b–2e present an example when THA did not observe plumes as it passed the magnetopause on the outbound portion of the orbit just dawnward of local noon. In these crossings, the magnetic field in the magnetosheath was northward (Figure 2b) and the magnetopause was identified by a change in the ion energy spectrum (Figure 2c). The black curve in Figure 2c marks the proton energy corresponding to the plasma bulk velocity. No cold ions were identified, indicating that no plume was present at the magnetopause at least at the spacecraft longitude. This indication is supported by the plasma density measurements (Figure 2e), where the ion density and the density inferred from spacecraft potential were both an order of magnitude lower than the outbound pass discussed below.

In contrast, Figures 2f–2i display an example when dense plasma was present at the magnetopause. As THD passed through the boundary, the magnetic field rotated from south to north (Figure 2f), and the ion spectrum displayed a change from the dense cool magnetosheath to warmer dayside plasma sheet proper (Figure 2g). In addition to the dayside plasma sheet population, a second population of ions was observed

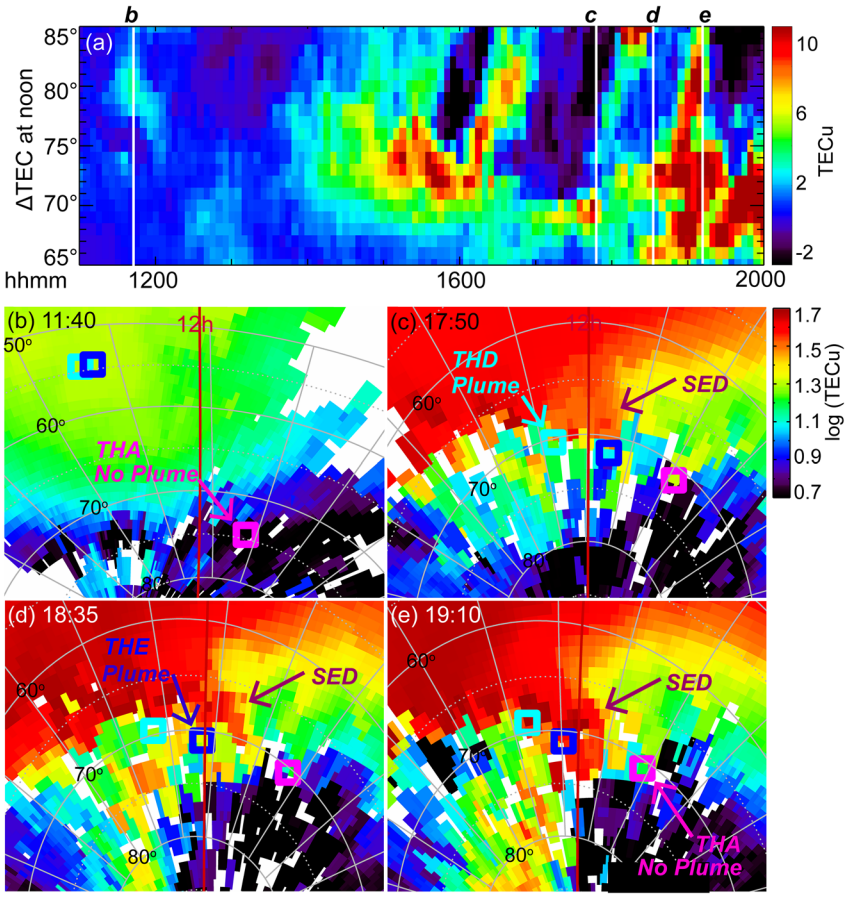

Figure 3. (a) Time series plot of background-subtracted TEC at 10–14 h MLT. The white lines overlain mark time instances when THEMIS spacecraft crossed the magnetopause. (b)–(e) Polar plots of TEC measurements with magnetic noon to the top. The gray contours mark latitudes and longitudes in geomagnetic coordinates. Footprints of THEMIS spacecraft based on T01 model are shown as open squares, which are colored coded in the same manner as Figure 2a. Spacecraft that detected plumes are labeled as "plume," otherwise labeled as "no plume.".

at energies of several to several tens of eV. This population was characterized by a narrow spectral peak (color-coded in red) with an energy consistent with what is expected from the plasma bulk velocity (black curve), suggesting that it was a plasmaspheric plume accelerated in the spacecraft reference frame. Note that the black curve is computed by assuming the ions to be protons only, whereas plumes often contain He^+ and O^+ especially during geomagnetically active times (Berube et al., 2005). These heavy ions may plausibly account for the secondary ion fluxes above the black curve (color coded in yellow and green).

The plume can also be confirmed by the high ion density and the high density from the spacecraft potential inside the magnetosphere (Figure 2i). In fact, the density averaged over a 20-s window immediately inside the magnetopause was 49 and 59 cm^{-3} according to the ion density and spacecraft potential, respectively, whereas it was 11 and 16 cm^{-3} immediately outside the boundary in the magnetosheath.

3.1.2. Connection Between SED and Plasmaspheric Plume

Here we examine whether the SED observed by GPS in Figure 1e and the plume by THEMIS in Figure 2 were coupled phenomena. Figure 3a presents TEC data near the magnetic noon in a similar format to Figure 1e, but in Figure 3a the data were background subtracted to enhance relative variations in time. The background at a given latitude and longitude location was defined as a three-hour running average of the TEC value at that location. With the subtraction, much of the positive storm effects at mid latitudes were removed because they were comparatively steady, whereas the TOI/patches (of ≥4 TECu in this background-subtracted plot) were enhanced because they excursed into the polar cap in a bursty manner. Note

that the TOI/patches originated from a region with elevated plasma density equatorward of the dark polar cap, and this elevated density corresponds to the dayside cusp. Its presence was overshadowed in Figure 1e by the positive storm effects.

The white lines overlain on Figure 3a mark time instances when THEMIS spacecraft crossed the magnetopause, including the two crossings shown in Figure 2. Two-dimensional maps of TEC (obtained at 5 min cadence) and the conjunction geometry at those time instances are shown in Figures 3b–3e. Figure 3b was taken at 1140 UT before the storm commenced, and the map shows a gradual decrease in TEC from mid to high latitudes, and from dayside to nightside, which is a typical distribution as expected from photo-ionization. No SED occurred. Around this time THA passed the magnetopause, and the spacecraft footprint is marked as the magenta square in Figure 3b. THA did not observe any plumes at the magnetopause either (Figures 2b–2e), suggesting a simultaneous absence of SED and plumes.

Figures 3c–3e were taken around the peak of the storm activities (Figure 1a) and the positive storm effects produced high plasma density at mid latitude. Extending from the midlatitude high density plasma was a horn-shaped high-density structure that stretched toward 71° MLAT and magnetic noon. This structure is a clear SED. The horn shape is consistent with SED being transported by plasma convection flows, which turn from sunward-directed, in sub-auroral latitudes, to poleward-directed, in the convection throat mapping to the cusp. THD, THE, and THA crossed the magnetopause successively and their footprints are labeled in Figure 3. At 1750 UT (Figure 3c), THD was magnetic conjugate to the SED, and it observed a plume at the magnetopause (Figures 2f–2i). Similarly, at 1835 UT (Figure 3d) THE was also magnetic conjugate to the SED, and it observed a plume (not shown). These two snapshots imply a simultaneous occurrence and collocation between the SED and the plume.

At 1910 UT (Figure 3e), THA did not observe a plume (not shown), whereas SED still occurred in the ionosphere. By inspecting the footprint of THA we find that THA was positioned at a longitude outside the SED and had likely missed the plasmaspheric plume that contacted the magnetopause. Therefore, an absence of plumes in spacecraft data may not necessarily suggest that no plumes have occurred. Instead, plumes may still occur at other longitudes.

To further corroborate the connection between the SED and the plasmaspheric plumes, we examine whether the physical mechanism that links the SED and the plume, which is SAPS, occurred. Two DMSP satellites, F17 and F16 crossed the dusk sector just before and after the SED/plume observation in Figure 3c. This SED/plume was selected because, as seen below, it was associated with favorable radar backscatter echoes and hence permits the investigation of its impact on dayside reconnection. The SAPS observations are representative for all dusk sector crossings during ~1500–1900 UT. After 1900 UT, SAPS continued to persist for one DMSP orbit, but at a weaker strength, and then disappeared.

Figures 4a–4e present measurements made by DMSP F17. The equatorward boundary of the ion precipitation was equatorward than that of the electrons (Figures 4d and 4e), and the offset took place within the downward region 2 field-aligned current (B_{azim} increasing toward higher latitudes in Figure 4c). These form a favorable condition for SAPS to occur, because the low ionospheric conductivity in the ion-only precipitation region calls for a large polarization electric field to close the downward region 2 field-aligned current (Anderson et al., 2001). Consistent with this expectation, we observe westward flows of ~1,000 m/s (Figure 4b) equatorward of the electron precipitation and within the Region 2 current, and these flows are SAPS. The SAPS was coincident with a depletion in ionospheric electron density at 60°–64° MLAT (Figure 4a), which is the ionospheric *trough*. The occurrence of the trough suggests that the frictional heating of SAPS has led to enhanced plasma temperatures and hence increased ionospheric recombination rates. DMSP F16 observed very similar features to F17 (Figures 4f–4j).

The collocation of SED and plumes, and the occurrence of SAPS, give strong evidence that the SED and the plume structures measured on January 17, 2013 were interconnected and were manifestations of the geospace plume that threads the ionosphere and the magnetosphere. We, therefore, can use SED as a remote sensing tool to infer when and where the plumes countered the magnetopause, so as to investigate whether and how reconnection is affected by the plumes.

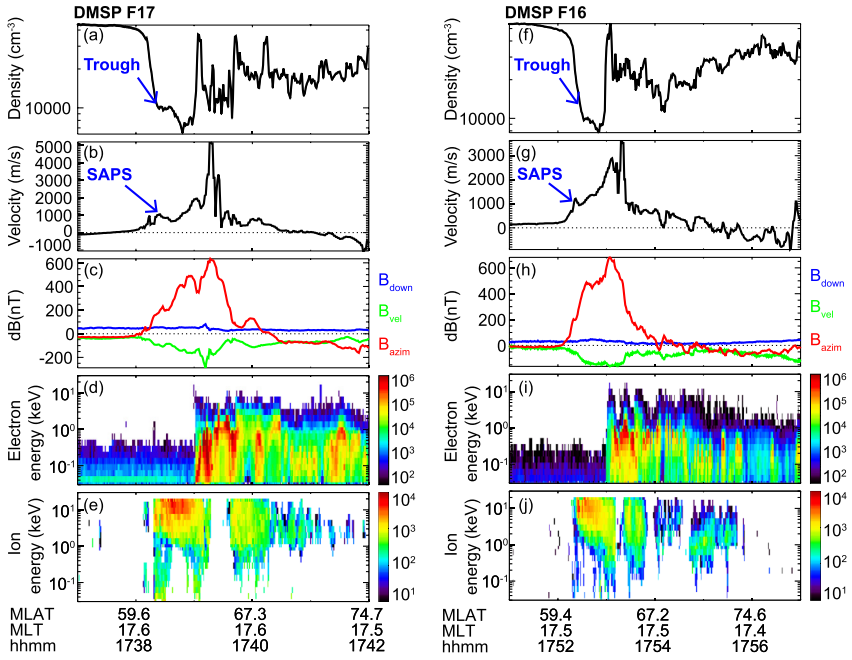

Figure 4. (a–e) In situ plasma density (at ~845 km altitude), cross-track velocity (positive values indicating westward flows), the magnetic field perturbations (an increase in the azimuthal direction toward higher latitudes indicating downward field-aligned currents), and the energy spectrum of the precipitating electrons and ions measured by DMSP F17. (f–j) Similar to (a–e) but showing measurements of F16.

3.1.3. Impact of Geospace Plume on Dayside Reconnection

As mentioned above, the geospace plume in Figure 3c was associated with favorable radar backscatter echoes and hence permits the investigation of its impact on dayside reconnection. Figure 5 presents a sequence of snapshots that capture the SuperDARN velocity field (left column) and the SED evolution (right column) as the SED extended toward the OCB. The SuperDARN spectral width data used to derive the OCB are presented in Figure 6, which shows that the OCB was located around 71°–72° MLAT. The 71° MLAT was marked as black (left column) and white (right column) arcs in the figure. Here we mostly focus on radar data around the magnetic noon and the pre-noon sectors as this is where radar backscatter echoes (color tiles) were dense, and we look for velocity vectors directed poleward from the OCB.

The interval of interest started from 1722 UT because before this time the radar backscatter echoes were limited. At 1722 UT, the SED extended to the OCB at 12–13 h MLT, as circled in red (Figure 5b). The LOS measurements captured a fast poleward-directed flow centered at 11 h MLT extended from the OCB, and the velocity vectors reveal that this flow spanned 10–12 h MLT, as circled in magenta. At 12–13 h MLT, that is, where the SED extended to the OCB, the velocity vectors were small, indicating that reconnection was locally weak.

As time elapsed, the portion of the SED extending to the OCB became broader and broader in local time, and by 1817 UT (Figures 5i and 5j) it spanned 9.5–14.5 h MLT. Correspondingly, the fast poleward directed flow, as seen in both the LOS and vector velocities, moved westward as if it was displaced by the SED. Specifically, the eastern boundary of the flow was displaced from 12 h MLT at 1722 (Figure 5a), to 10 h MLT at 1817 UT (Figure 5i), coinciding with the westward expansion of the SED. This apparent displacement corresponds to a suppression of plasma flows at regions where the SED extended to the OCB and an enhancement of flows adjacent to the SED. Since the flows across the OCB are directly driven by magnetopause reconnection, the observation suggests that the efficiency of reconnection was reduced where the SED extended to the OCB, and enhanced in the surrounding. Mapped to the magnetopause, this means the efficiency of reconnection would be suppressed where the dense plume contacted the boundary and increased in adjacent regions.

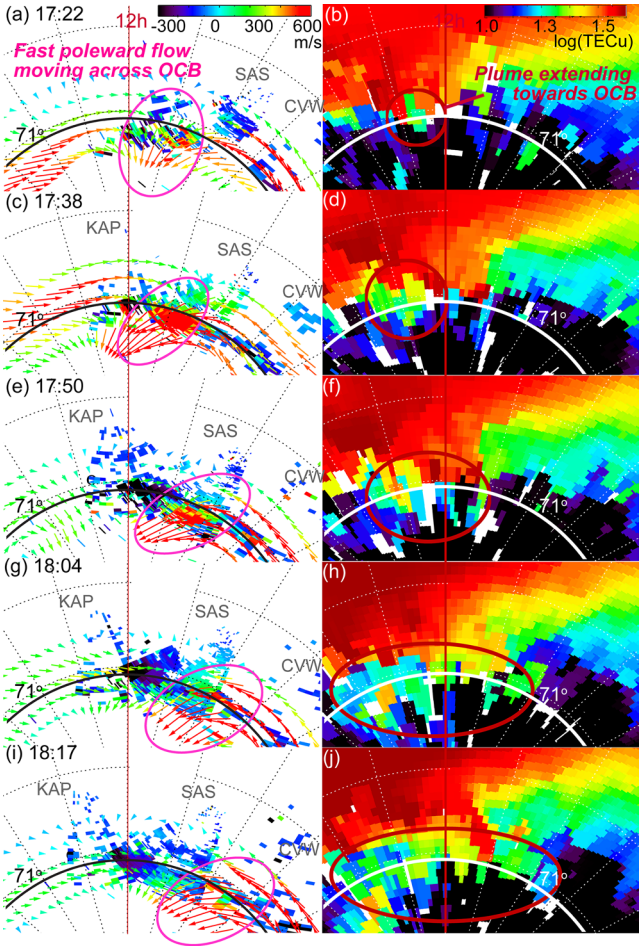

Figure 5. (Left column) Maps of plasma convection plotted in geomagnetic latitude-MLT coordinates with magnetic noon at the top. The color tiles represent line-of-sight velocity measurements and the corresponding radar are labeled in gray. Positive values represent plasma moving away from the radar. The color arrows represent the spherical harmonic fitted velocity vectors. To reduce the clutter, the velocity vectors (color arrows) are plotted with a spatial resolution of 2° in latitude and longitude, and only those around the open-closed field line boundary (OCB) latitude are shown. The OCB latitude is indicated. Regions of fast poleward flows moving across the OCB are highlighted with magenta circles. (Right column) Maps of TEC plotted in geomagnetic latitude-MLT coordinates with magnetic noon at the top. The OCB latitude is indicated. Portions of storm enhanced density extends to the OCB are highlighted with red circles. The red vertical line on the TEC maps on the right represents local noon.

The change in reconnection activity can also be seen from the time series plot in Figure 6. The IMF showed a sharp southward turning at 1700 UT, after which it stayed steady. The steadiness implies that the change in the dayside plasma convection was not externally driven but reflects changes from the magnetosphere, such as the introduction of a dense geospace plume. The black curve in Figure 6b marked the spectral width at 250 m/s as a proxy of the OCB. We chose this threshold because it was the middle point between the ~<100 m/s spectral width at low latitudes and the ~>400 m/s spectral width at high latitudes, and using other thresholds would only adjust the OCB location by several tenths of 1°. The OCB was positioned steadily at ~71–72° MLAT, especially during 1720–1820 UT which is the interval of our interest. Since the OCB did not exhibit significant motion, the strength of plasma flows dominate the local reconnection rate.

Figures 6c and 6d display the LOS measurements made by Saskatoon (SAS) and Christmas Valley West (CVW) radars, respectively, and the former was positioned to the east of the latter as labeled in Figure 5. The LOS velocities sharply decreased at SAS longitude at 1750 UT (Figure 6c), whereas increased simultaneously at CVW longitude (Figure 6d). By referring to Figure 5e, we find that the variation can be explained by the westward expansion of the SED, where it suppressed the convection from 11 h MLT to the post-noon sector beyond the radar backscatter echoes and enhanced the convection at 9.5–11 h MLT.

The suppression of reconnection-related flow at the dense plume plasma has been predicted by both the local- and global-control theories of solar wind-magnetosphere coupling, but the two theories diverge in predicting whether the reconnection adjacent to the plume changes. No change in adjacent regions is expected for a system that purely follows local control. A global control or mixed model would predict enhancements in the efficiency of reconnection in regions adjacent to a plume due to the pile up of magnetosheath field lines. The observation of an enhanced flow adjacent to the SED is consistent with the global- or mixed-control model.

Figure 6e shows the CPCP, which is a proxy of the globally integrated reconnection rate. Unfortunately, we find that the variation trend of CPCP was not coupled to the evolution of the studied SED in a straightforward manner, making it difficult to assess whether and how much the plume impacted the integrated reconnection. Nevertheless, the CPCP was initially ~70 kV and started to increase at ~1715 UT. It reached maximum at 1738 UT at ~95 kV and returned to its initial value. On the other hand, the SED arrived at the pre-noon OCB at 1725 UT, when the CPCP showed an increase. As the SED spread in longitude, the CPCP first continued to increase and then decreased. We postulate the reason for the mismatch between the SED and CPCP evolution is due to the southward IMF turning. Studies suggest that the adjustment in convection to IMF turnings occurred in the dayside cusp first and then propagates toward the nightside over a period of ~10 min (Cowley & Lockwood, 1992; Etemadi et al., 1988; Khan & Cowley, 1999; Lockwood & Cowley, 1999; Lockwood et al., 1986; Saunders et al., 1992; Todd et al., 1988), and the adjustment in total takes from 12 to 30 min before a new steady state pattern is established (Hairston & Heelis, 1995; McWilliams et al., 2000, 2001; Ruohoniemi & Greenwald, 1998). In the following section, we analyze a geospace plume event under a prolonged steady IMF condition to investigate the impact of plumes on the integrated global reconnection rate.

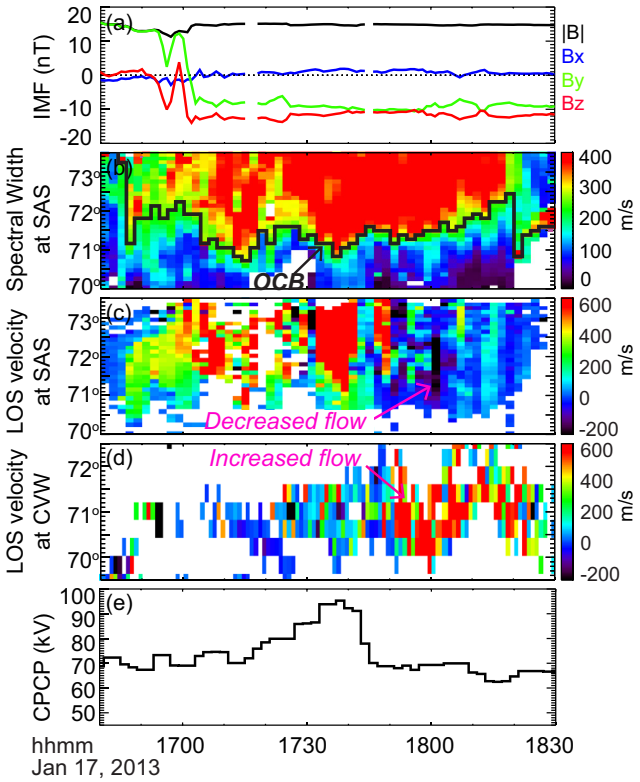

Figure 6. (a–e) OMNI IMF, SuperDARN spectral width measured by Saskatoon (SAS) radar, line-of-sight (LOS) velocity by SAS radar, LOS velocity by Christmas Valley West (CVW) radar, and cross polar cap potential (CPCP). The SAS measurements are averages between Beams 8–11 and the CVW measurements are averages between Beams 20–23. The OCB is identified with a threshold of 250 m/s and is outlined by the black line in Panel (b). Positive LOS velocity indicate flows moving away from the radar.

3.2. Geospace Plume on October 11, 2010

3.2.1. Occurrence and Interconnection of SED and Plasmaspheric Plume

The occurrence and interconnection of SED and plasmaspheric plumes on October 11, 2010 shared great similarities with the first event, and hence here we only outline the key features to minimize repetition. Figure 7 presents an overview of the event. The storm initiated at 0450 UT coincident with the increase in the solar wind density, and reached its peak activity at 1855 UT. The minimum value of the SYM-H index was −76 nT, suggesting that the storm, similar to the first event, was moderate in intensity. The main phase of the storm was associated with prolonged southward IMF. The solar wind velocity was steady and stayed at ∼350 km/s. The magnetosonic Mach number was overall high (>4) except for 1000–1300 UT. The high Mach number implies that the global force balance that controls the magnetosheath flow pattern was dominated by the pressure gradient force in this event (Lopez & Gonzalez, 2017; Lopez et al., 2010). TEC measurements exhibit an increase in electron density at mid latitude during the storm main phase. We can identify SED during periods when they extended into the polar cap forming TOI and/or polar cap patches, that is, as features extending from the midlatitude density enhancement and moving into the otherwise low-density polar cap region during 1300–2000 UT.

Calibrated LANL MPA data are available for this event and are presented in Figures 8a and 8b. The figures show the cold ion densities measured by spacecraft L01, L02, L04, and L97 along their geosynchronous orbits. The densities are taken from 2-h intervals that are centered around the times when THEMIS spacecraft passed the magnetopause, so that the two data sets reflect the plume activity around the same time. Following statistical measurements by Sheeley et al. (2001), the plasmaspheric density at geosynchronous orbits should to be >10 cm^{-3}. Plasma with a density >10 cm^{-3} was detected during 12–14 UT by L02 and L94, which were positioned in the dusk and afternoon sectors, respectively. The density at the nightside sector was low. Such a distribution suggests that a plasmaspheric material extended outward in a plume in the dusk/afternoon sector. No high density plasma was detected in the time period 22–24 UT, suggesting that no plasmaspheric plasma was being transported through the geosynchronous orbit, at least at the spacecraft local time.

Figures 8c–8j display THEMIS measurements as the spacecraft passed the magnetopause on their outbound (left) and inbound (right). Dense plume material was observed during the outbound pass, as evidenced by the narrow ion energy spectral peaks that were well traced by the plasma kinetic velocity (Figure 8d), and the high plasma density of ∼20 cm^{-3} inferred from the spacecraft potential (Figure 8f). A similar density is obtained from the ESA ion density measurement when the bulk velocity was large enough to exceed the energy threshold of ESA.

On the other hand, no dense plume-like material was measured at the magnetopause upon the prenoon inbound pass, consistent with LANL observations. ESA did not see narrow peaks in the ion energy spectrum even though there were instances when the bulk velocity was large enough to exceed the energy threshold of ESA, such as during ∼22:40:30–22:42:15 and ∼22:43:15–22:43:35 UT (Figure 8h). The ion density and the density inferred from spacecraft potential were both low, of ∼3 cm^{-3}.

When LANL and THEMIS observed the plume in the magnetosphere, TEC measurements captured SED in the ionosphere (Figure 8k). Here the TEC map contained data gaps because the GPS receiver network at this time was not as dense as the first event. Nevertheless, we can still clearly identify a SED structure which extended from the midlatitude high density region to 71° MLAT where the OCB was positioned, and

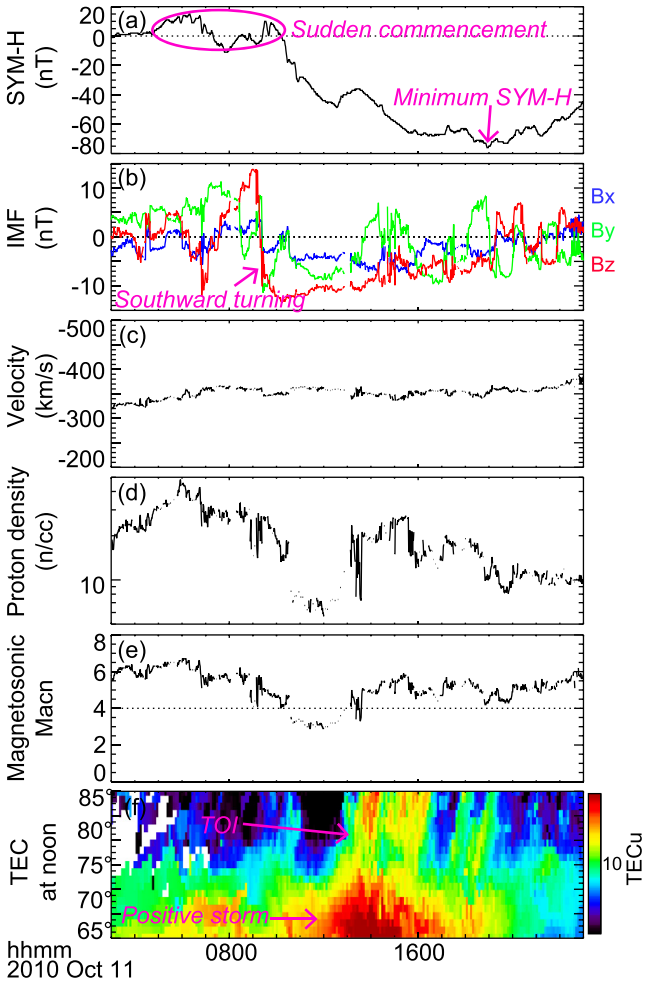

Figure 7. Similar to Figure 1 but showing conditions on October 11, 2010.

the extension occurred at a longitude coincided with that of the THEMIS footprint. In addition to being collocated with the plume, the SED was accompanied by SAPS electric field (not shown) similarly to the first event, which implies a connection in the cold plasma motion in the ionosphere and plasmasphere through $E \times B$ drift. The SED and plume were therefore manifestations of the same geospace plume in the ionosphere and magnetosphere, respectively. On the other hand, when LANL and THEMIS did not observe the plume in the magnetosphere, TEC measurements also suggested an absence of SED (Figure 8l).

3.2.2. Impact of Geospace Plume on Dayside Reconnection

Figure 9 presents a sequence of snapshots that capture the SuperDARN velocity field (left column) and the SED evolution (right column) as the SED extended to the OCB. The SED under analysis is the same as the one in Figure 8k. The OCB was located at 71° MLAT around noon and 68° MLAT around 16 h MLT, and was drawn in black and magenta in the left and right column of the figure, respectively (here we have assumed that the OCB had an oval shape). Although the OCB is determined based on the SuperDARN spectral width measurements, and it is also roughly consistent with being the poleward boundary of the sunward flow occurring in the closed field line region. Because the radar backscatter echoes were available in the post-noon sector, we focus on the velocity vectors there.

At 1145 UT before the arrival of the SED (Figure 9b), a fast poleward directed flow extended from the OCB at 12–14 h MLT (Figure 9a), implying that reconnection proceeded efficiently at that local time. At 1212 UT, a SED structure started to develop and extended to the OCB (highlighted with a dotted magenta circle in Figure 9d). The somewhat low electron content is probably because the positive storm effects just commenced at mid latitude and the associated electron density had yet built up.

With time the electron content of the SED increased, and at 1237 and 1250 UT the SED appear as red-colored tongue structure extending to the OCB (Figures 9f and 9h) at 11–13 h MLT. The flow at this local time decreased significantly, from ~500 to 600 m/s at 1145 UT to ~200 m/s at 1250 UT, whereas the flow to the east enhanced to ~600 m/s. The result is that the fast poleward flow region, which corresponds to high reconnection rate and was circled in magenta, displaced from 12 to 14 h MLT at 1145 UT to 14–16 h MLT at 1250 UT. This indicates that reconnection was enhanced adjacent to the plume at the magnetopause, once again consistent with a global- or mixed solar wind-magnetosphere coupling theory.

Such an impact on reconnection can also be deduced from the time series plot in Figure 10. The IMF was steady throughout the interval of our interest (Figure 10a), and therefore the change in dayside reconnection should not be driven externally by the IMF but reflects the impact of the geospace plume. The OCB is determined as the 150-m/s spectral width boundary, and its location was steady (Figures 10b and 10d), implying that the local reconnection rate was controlled by the plasma flow velocity. The LOS velocity at PYK showed an overall decrease at 1230 UT, whereas that at HAN station showed an increase, corresponding to a suppression of reconnection activity close to the SED and an enhancement away from it.

Figure 10f displays the CPCP during this event. Despite the redistribution of the strength of reconnection associated with the plume, the CPCP was steady, and therefore the plume did not change the integrated reconnection rate. This finding is consistent with a global-control model, where the integrated reconnection rate depends on the solar wind driving rather than local physics.

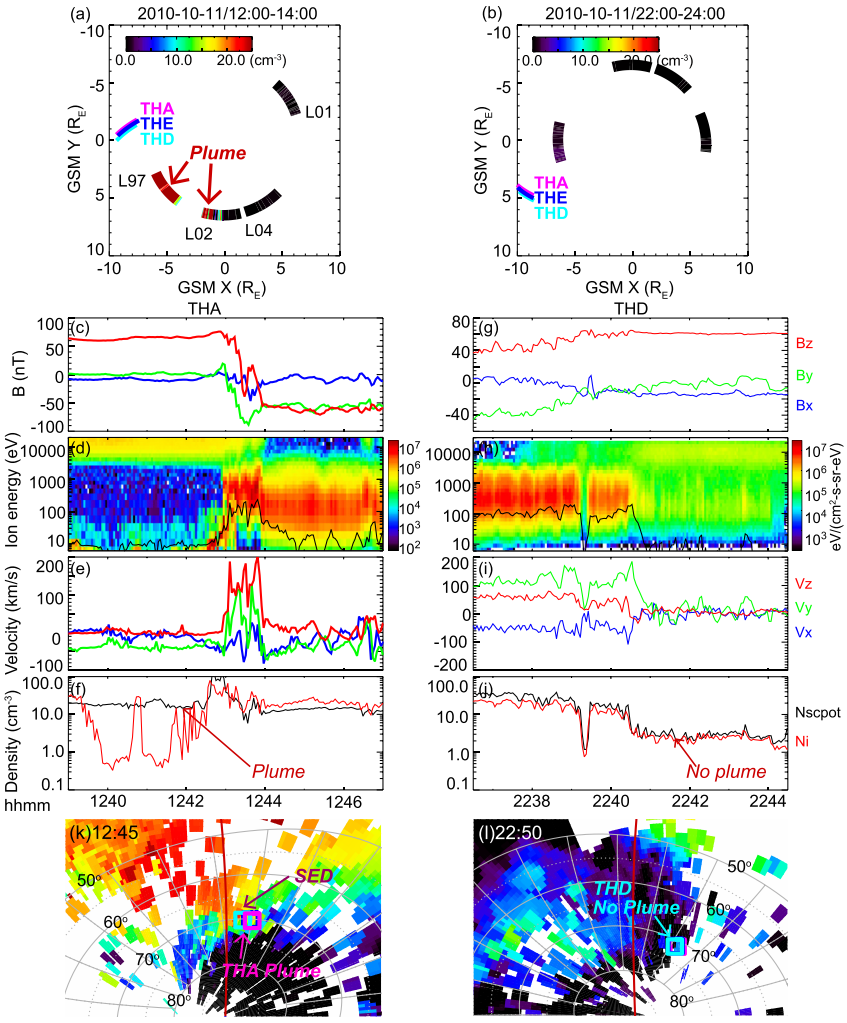

Figure 8. (a–b) Cold ion densities measured by spacecraft L01, L02, L04, and L97 along their geosynchronous orbits during 2-h intervals indicated at the top of the figures. The densities are colored according to the color scale. THEMIS spacecraft locations are also shown. (c–l) Similar to Figure 3 but showing measurements on October 11, 2010.

4. Discussion

4.1. Effect of Plumes on Local Reconnection Rate

In this section, we discuss the effect of plumes on local reconnection rate because, although both local- and global-control theories predict a decrease effect, the magnitude of decrease we observe is significantly larger than many of the existing reports. For example, Wang et al. (2015) found that the decrease of the reconnection rate due to cold ion and O^+ mass loading is only up to 10%–20%. Fuselier et al. (2017) found that among the time when plumes are detected, only 15%–38% of the time do plumes decrease the reconnection rate by >20%, and that the maximum decrease is by 35%. Considering that Wang et al. (2015) and Fuselier et al. (2017) draw their conclusions from observations made by CLUSTER and MMS spacecraft, respectively, whereas we use ground-based SuperDARN, one may wonder whether the reconnection activity remotely sensed by SuperDARN is consistent with what happens in situ.

To answer this question, we follow the methodology of Fuselier et al. (2017) to estimate the in situ reconnection rate. Fuselier et al. (2017) computed the fractional reduction of the local dayside reconnection rate due to a nonzero magnetospheric ion density as

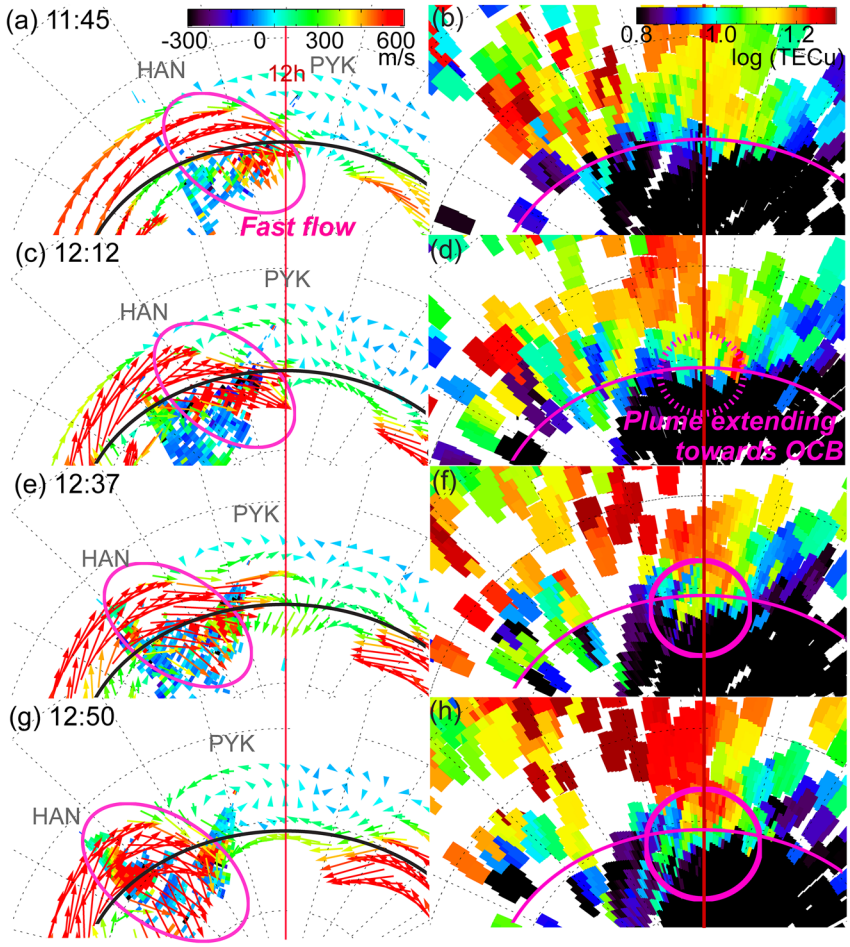

Figure 9. Similar to Figure 5 but showing measurements on October 11, 2010.

$$R = \frac{\left(\rho_s B_M\right)^{1/2}}{\left(\rho_M B_s + \rho_s B_M\right)^{1/2}}$$

where R is the reconnection rate normalized to the reconnection rate if there were no magnetospheric ions present in the magnetosphere, ρ is the mass density, B is the reconnecting component of the magnetic field. The subscripts "M" and "S" refer to the magnetosphere and magnetosheath, respectively. R can be rewritten as (Fuselier et al., 2016)

$$R = \left(1 + \mathrm{MC}\right)^{-1/2}$$

where the mass correction factor, MC, is defined as

$$\mathrm{MC} \equiv \frac{\rho_M B_S}{\rho_S B_M}$$

R can, therefore, be derived from plasma and magnetic field measurements made during our THEMIS magnetopause crossings. However, different from MMS, THEMIS cannot resolve plasma composition, and hence cannot provide a definitive mass density. We assume three extreme scenarios where the plume was constituted of protons only, He^+ only, and O^+ only. Although none of these scenarios are realistic, they constrain the range of the reconnection rate decrease, and can hence be used to evaluate the fidelity of SuperDARN remote sensing. Borovosky et al. (2013) assumed a plasmasphere composition mix with 77% H^+,

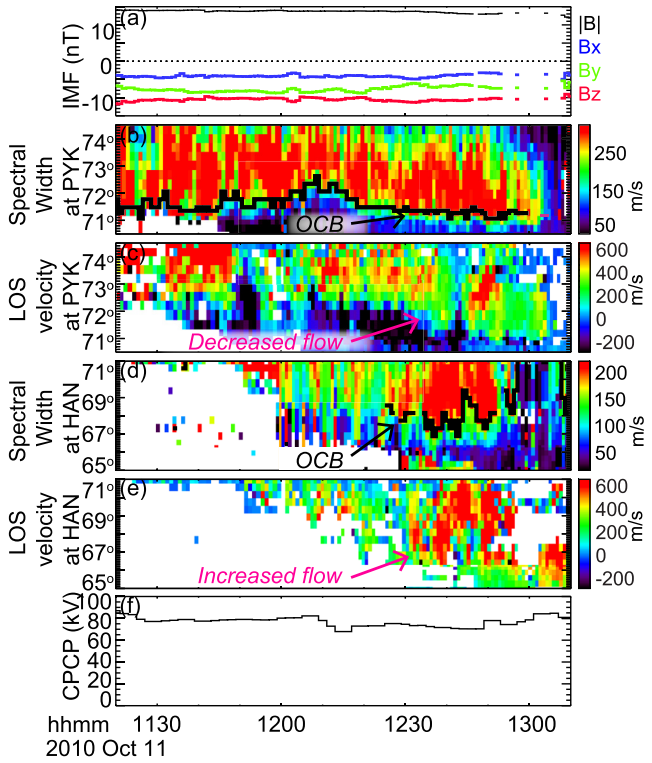

Figure 10. Same as Figure 6 but showing measurements on October 11, 2010. The PYK line-of-sight (LOS) velocity is an average between Beams 1–4, and HAN LOS velocity is average between Beams 6–8.

20% He^+, and 3% O^+, which we also include in our computation as one potentially realistic scenario. Plasma in the magnetosheath is assumed to consist of protons and He^+. The He^+ concentration is taken either from the upstream ACE measurements, or as 4% when ACE data are not available. The plasma number density (from spacecraft potential) and magnetic field are taken as the averages of 20-s interval inside and outside the magnetopause, and are listed in Table 1. The MC and *R* values are also shown in Table 1.

For the January 17, 2013 event, the in situ local reconnection is estimated to be reduced by 60%, 79%, and 89% for plumes constituted of protons, He^+ and O^+, respectively. Therefore, even the proton-only plume results in a significant decrease by 60% in the local reconnection rate, and considering that plumes during geomagnetically active times often contain substantial He^+ and O^+ (Berube et al., 2005), the actual decrease must be >60%.

This measurement-based calculation above is then compared with the more direct measurement of the change in reconnection based on SuperDARN measurements. The SuperDARN values are presented at the bottom of Table 1. As mentioned in Section 2, the reconnection rate is estimated as magnetic flux transfer across the OCB in the frame of the OCB. We first select a local time that had good radar backscatter echoes and was affected by the SED, and extract the northward component of the plasma velocity at that local time from the convection maps. The local time range is selected to be 11–12 h MLT for the January 17, 2013 event. The plasma velocity is then transferred to the OCB frame where the instantaneous OCB motion is obtained by tracing the spectral width boundary (Figure 6). The final velocity, when multiplied by the terrestrial magnetic field, gives the reconnection electric field.

To reflect how much the reconnection rate changed in association with the plume, we compare the minimum and maximum reconnection electric fields over the time interval of our interest (1720–1820 UT). SuperDARN suggests that the minimum reconnection electric field was 4.7 mV and the maximum was 25.3 mV. The ratio of the two is therefore 19%. This implies reconnection was reduced by 81% at the location of the plume, similar to the prediction of a He^+-only plume, implying that the SuperDARN remote sensing is sensible. The minimum reconnection rate occurred at 17:50 UT, only 4 min after THD magnetopause crossing.

The plume on October 11, 2010 was not as dense as the one on January 17, 2013, and the in situ reconnection is estimated to be reduced locally by 37%, 62%, and 80% for plumes constituted of protons, He^+, and O^+. SuperDARN measurements suggest reconnection was reduced locally by 68%, which is again comparable to a He^+-only plume.

Therefore, both remote and in situ observations indicate that plumes can substantially decrease the local reconnection rate as long as the plume density is sufficiently large. Interestingly, the two studied geospace plume events occurred during moderate storms, implying that major storms are not required for such a substantial decrease to occur. Also note that although the reconnection rate was decreased, reconnection still proceeded at the location of the dense plume material. As seen from Figures 2h and 8f, Alfvenic reconnection jets occurred at the magnetopause in association with the plumes. In the conjugate ionosphere, plasma still moved poleward across the OCB.

4.2. Effect of Plumes on Global Reconnection Rate

The observed plume effect agrees with the prediction of the global-control theory that the local reconnection rate should increase in regions adjacent to plumes for both low and high Mach numbers. Below we compare the plume effect with the predictions of the mixed-control theory proposed by Zhang et al. (2016, 2017) and

Table 1
In Situ Magnetic Field (B) and Plasma Density (n) Averaged Over 20-s Intervals Immediately Outside the Magnetopause, as Well as the Associated Mass Correction Factor (MC) and Normalized Reconnection Rate (R)

		January 17, 2013	October 11, 2010
		Magnetopause crossing at ~17:46 UT made by THD	Magnetopause crossing at ~12:44 UT made by THA
	B_S	−58	−76
	B_M	38	64
	n_S	16	13
	n_M	59	18
Proton plume	MC	5.3	1.5
	R	0.40	0.63
He^+ plume	MC	21.2	5.9
	R	0.21	0.38
O^+ plume	MC	85.0	23.5
	R	0.11	0.20
Realistic plume	MC	12.2	3.4
	R	0.28	0.48
Super-DARN	R	0.19	0.32

Notes. The subscripts "M" and "S" refer to the magnetosphere and magnetosheath, respectively. The magnetic field is the reconnecting component determined through the minimum variance analysis. Also shown is the variation of reconnection rate estimated based on SuperDARN.

Ouellette et al. (2016). These authors propose that both the global- and local-control theories apply and that the two theories have different validity domains. The global-control theory is valid when there is a small amount of mass loading at the dayside magnetopause, whereas the local-control theory is valid when there is a large amount of mass loading. In the specific simulation setup of Zhang et al. (2017), the transition happens when the atomic mass at the magnetopause inflow region is 8–16 amu/cm^3.

The similarity between the observed decrease of the local reconnection rate and the prediction of a He^+-only plume implying that our plumes had an ion atomic mass of about 4 amu. This, when combined with the number density, implies a mass loading of about 236 and 72 amu/cm^3 for the two storms, both falling into the domain where the local-control theory is proposed to be valid. Although our observations do not exclude a mixed-control theory, they imply that the global-control theory can be valid for a larger range of mass loading than what Zhang et al. (2017) proposed and it awaits to be tested how much mass loading is needed for the local-control theory to dominate.

5. Conclusion

We examine geospace plume and its impact on dayside magnetopause reconnection rate using a distributed observatory consisting of THEMIS, LANL, and DMSP satellites, GPS network, and SuperDARN radar network. The geospace plume events are selected based on plasmaspheric plumes in the magnetosphere, and SED in the ionosphere. During the studied two moderate storms, one associated with low Mach number and the other with high Mach number, the plasmaspheric plumes and the SED occurred simultaneously and were magnetically conjugate. The plasma motion was connected through $E \times B$ drift associated with the SAPS electric field. The SED and the plumes were therefore interconnected and were manifestations of the geospace plume.

In the ionosphere, as the SED extended to the separatrix (or OCB), flows moving across the OCB got suppressed and the local reconnection rate decreased by 81% and 68% in the two storm events, respectively. The amount of decrease is consistent with the mass loading effect of the plume if the plume's atomic mass was ~4 amu. Although suppressed, reconnection still proceeded at the plume longitude. Adjacent to the plume, reconnection was enhanced, and when the SED spread along the separatrix azimuthally, the region of the enhancement also shifted so that it was always positioned adjacent to the SED. When the solar wind driving was stable, little variation was seen in the CPCP, implying that the global reconnection rate remained steady. Such observations are consistent with the global-control theory.

Data Availability Statement

LANL data were provided by Michael G. Henderson (http://mghenderson@lanl.gov) and can be accessed through http://zenodo.org/record/4670432#.YG3jvWVKiK8. Data for the TEC processing are provided from the following organizations: UNAVCO; Scripps Orbit and Permanent Array Center; Institut Géographique National, France; International GNSS Service; the Crustal Dynamics Data Information System (CDDIS); National Geodetic Survey; Instituto Brasileiro de Geografia e Estatística; RAMSAC CORS of Instituto Geográfico Nacional de la República Argentina; Arecibo Observatory; Low-Latitude Ionospheric Sensor Network (LISN); Topcon Positioning Systems, Inc.; Canadian High Arctic Ionospheric Network; Institute of Geology and Geophysics, Chinese Academy of Sciences, China Meteorology Administration; Centro di Ricerche Sismologiche; Système d'Observation du Niveau des Eaux Littorales (SONEL); RENAG: REseau NAtional GPS permanent; GeoNet New Zealand; and GNSS Reference Networks. PFISR operations are supported by NSF cooperative agreement AGS-1133009 to SRI International, and data are available from

http://amisr.com/database or http://isr.sri.com/madrigal. SuperDARN data are available through http://vt.superdarn.org/. DMSP data are available through https://www.ngdc.noaa.gov/stp/satellite/dmsp/

Acknowledgments
This work was supported by NSF grant AGS-2025570 and NASA Grant 80NSSC21K0003. Xueling Shi and John M. Ruohoniemi acknowledge the support of NSF through awards AGS-1341918 and AGS-1935110. The THEMIS mission is supported by NASA contract NAS5-02099 and NSF grant AGS-1004736 and data are available http://themis.ssl.berkeley.edu/index.shtml. GPS TEC data products and access through the Madrigal distributed data system (http://isr.sri.com/madrigal/) are provided to the community by the Massachusetts Institute of Technology under support from U.S. National Science Foundation grant AGS-1242204. The authors acknowledge the use of SuperDARN data. SuperDARN is a collection of radars funded by national scientific funding agencies of Australia, Canada, China, France, Italy, Japan, Norway, South Africa, United Kingdom, and the United States of America.

References

Anderson, P. C., Carpenter, D. L., Tsuruda, K., Mukai, T., & Rich, F. J. (2001). Multisatellite observations of rapid subauroral ion drifts (SAID). *Journal of Geophysical Research*, *106*(A12), 29585–29599. https://doi.org/10.1029/2001JA000128

André, M., & Cully, C. M. (2012). Low-energy ions: A previously hidden solar system particle population. *Geophysical Research Letters*, *39*(3). https://doi.org/10.1029/2011GL050242

Archer, M. O., Hartinger, M. D., Walsh, B. M., Plaschke, F., & Angelopoulos, V. (2015). Frequency variability of standing Alfvén waves excited by fast mode resonances in the outer magnetosphere. *Geophysical Research Letters*, *42*(23), 10150–10159. https://doi.org/10.1002/2015GL066683

Auster, H. U., Glassmeier, K. H., Magnes, W., Aydogar, O., Baumjohann, W., Constantinescu, D., et al. (2009). The THEMIS fluxgate magnetometer. In J. L. Burch, & V. Angelopoulos (Eds.), *The THEMIS mission* (pp. 235–264). https://doi.org/10.1007/978-0-387-89820-9_11

Baker, K. B., Dudeney, J. R., Greenwald, R. A., Pinnock, M., Newell, P. T., Rodger, A. S., et al. (1995). HF radar signatures of the cusp and low-latitude boundary layer. *Journal of Geophysical Research*, *100*(A5), 7671–7695. https://doi.org/10.1029/94JA01481

Baker, K. B., Rodger, A. S., & Lu, G. (1997). HF-radar observations of the dayside magnetic merging rate: A geospace environment modeling boundary layer campaign study. *Journal of Geophysical Research*, *102*(A5), 9603–9617. https://doi.org/10.1029/97JA00288

Bame, S. J., McComas, D. J., Thomsen, M. F., Barraclough, B. L., Elphic, R. C., Glore, J. P., et al. (1993). Magnetospheric plasma analyzer for spacecraft with constrained resources. *Review of Scientific Instruments*, *64*, 1026–1033.

Berube, D., Moldwin, M. B., Fung, S. F., & Green, J. L. (2005). A plasmaspheric mass density model and constraints on its heavy ion concentration. *Journal of Geophysical Research*, *110*(A4). https://doi.org/10.1029/2004JA010684

Bonnell, J. W., Mozer, F. S., Delory, G. T., Hull, A. J., Ergun, R. E., Cully, C. M., et al. (2008). The electric field instrument (EFI) for THEMIS. *Space Science Reviews*, *141*, 303–341. https://doi.org/10.1007/s11214-008-9469-2

Borovsky, J. E., & Denton, M. H. (2006). Effect of plasmaspheric drainage plumes on solar-wind/magnetosphere coupling. *Geophysical Research Letters*, *33*(20). https://doi.org/10.1029/2006GL026519

Borovsky, J. E., Denton, M. H., Denton, R. E., Jordanova, V. K., & Krall, J. (2013). Estimating the effects of ionospheric plasma on solar wind/magnetosphere coupling via mass loading of dayside reconnection: Ion-plasma-sheet oxygen, plasmaspheric drainage plumes, and the plasma cloak. *Journal of Geophysical Research: Space Physics*, *118*(9), 5695–5719. https://doi.org/10.1002/jgra.50527

Borovsky, J. E., Hesse, M., Birn, J., & Kuznetsova, M. M. (2008). What determines the reconnection rate at the dayside magnetosphere? *Journal of Geophysical Research*, *113*(A7). https://doi.org/10.1029/2007JA012645

Buonsanto, M. J. (1995a). A case study of the ionospheric storm dusk effect. *Journal of Geophysical Research*, *100*(A12), 23857–23869. https://doi.org/10.1029/95JA02697

Buonsanto, M. J. (1995b). Millstone Hill incoherent scatter F region observations during the disturbances of June 1991. *Journal of Geophysical Research*, *100*(A4), 5743–5755. https://doi.org/10.1029/94JA03316

Buonsanto, M. J. (1999). Ionospheric storms—A review. *Space Science Reviews*, *88*(3), 563–601. https://doi.org/10.1023/A:1005107532631

Burns, A. G., Solomon, S. C., Wang, W., & Killeen, T. L. (2007). The ionospheric and thermospheric response to CMEs: Challenges and successes. *Journal of Atmospheric and Solar-Terrestrial Physics*, *69*(1), 77–85. https://doi.org/10.1016/j.jastp.2006.06.010

Cassak, P. A., & Shay, M. A. (2007). Scaling of asymmetric magnetic reconnection: General theory and collisional simulations. *Physics of Plasmas*, *14*(10), 102114. https://doi.org/10.1063/1.2795630

Chappell, C. R. (1974). Detached plasma regions in the magnetosphere. *Journal of Geophysical Research*, *79*(13), 1861–1870. https://doi.org/10.1029/JA079i013p01861

Chappell, C. R., Huddleston, M. M., Moore, T. E., Giles, B. L., & Delcourt, D. C. (2008). Observations of the warm plasma cloak and an explanation of its formation in the magnetosphere. *Journal of Geophysical Research: Space Physics*, *113*(A9). https://doi.org/10.1029/2007JA012945

Chen, A. J., & Grebowsky, J. M. (1978). Dynamical interpretation of observed plasmasphere deformations. *Planetary and Space Science*, *26*(7), 661–672. https://doi.org/10.1016/0032-0633(78)90099-5

Chen, A. J., & Wolf, R. A. (1972). Effects on the plasmasphere of a time-varying convection electric field. *Planetary and Space Science*, *20*(4), 483–509. https://doi.org/10.1016/0032-0633(72)90080-3

Chen, L., Thorne, R. M., Li, W., Bortnik, J., Turner, D., & Angelopoulos, V. (2012). Modulation of plasmaspheric hiss intensity by thermal plasma density structure. *Geophysical Research Letters*, *39*(14). https://doi.org/10.1029/2012GL052308

Chisham, G., & Freeman, M. P. (2003). A technique for accurately determining the cusp-region polar cap boundary using SuperDARN HF radar measurements. *Annales Geophysicae*, *21*(4), 983–996. https://doi.org/10.5194/angeo-21-983-2003

Chisham, G., & Freeman, M. P. (2004). An investigation of latitudinal transitions in the SuperDARN Doppler spectral width parameter at different magnetic local times. *Annales Geophysicae*, *22*(4), 1187–1202. https://doi.org/10.5194/angeo-22-1187-2004

Chisham, G., Freeman, M. P., Abel, G. A., Lam, M. M., Pinnock, M., Coleman, I. J., et al. (2008). Remote sensing of the spatial and temporal structure of magnetopause and magnetotail reconnection from the ionosphere. *Reviews of Geophysics*, *46*(1). https://doi.org/10.1029/2007RG000223

Chisham, G., Freeman, M. P., Coleman, I. J., Pinnock, M., Hairston, M. R., Lester, M., & Sofko, G. (2004). Measuring the dayside reconnection rate during an interval of due northward interplanetary magnetic field. *Annales Geophysicae*, *22*(12), 4243–4258. https://doi.org/10.5194/angeo-22-4243-2004

Chisham, G., Freeman, M. P., Lam, M. M., Abel, G. A., Sotirelis, T., Greenwald, R. A., & Lester, M. (2005). A statistical comparison of SuperDARN spectral width boundaries and DMSP particle precipitation boundaries in the afternoon sector ionosphere. *Annales Geophysicae*, *23*(12), 3645–3654. https://doi.org/10.5194/angeo-23-3645-2005

Chisham, G., Freeman, M. P., & Sotirelis, T. (2004). A statistical comparison of SuperDARN spectral width boundaries and DMSP particle precipitation boundaries in the nightside ionosphere. *Geophysical Research Letters*, *31*(2). https://doi.org/10.1029/2003GL019074

Chisham, G., Freeman, M. P., Sotirelis, T., & Greenwald, R. A. (2005). The accuracy of using the spectral width boundary measured in off-meridional SuperDARN HF radar beams as a proxy for the open-closed field line boundary. *Annales Geophysicae*, *23*(7), 2599–2604. https://doi.org/10.5194/angeo-23-2599-2005

Chisham, G., Freeman, M. P., Sotirelis, T., Greenwald, R. A., Lester, M., & Villain, J.-P. (2005). A statistical comparison of SuperDARN spectral width boundaries and DMSP particle precipitation boundaries in the morning sector ionosphere. *Annales Geophysicae*, *23*(3), 733–743. https://doi.org/10.5194/angeo-23-733-2005

Coster, A., Foster, J., & Erickson, P. (2003). Monitoring the ionosphere with GPS. *Space Weather*, *14*, 42–47.

Coster, A., & Skone, S. (2009). Monitoring storm-enhanced density using IGS reference station data. *Journal of Geodesy*, *83*(3), 345–351. https://doi.org/10.1007/s00190-008-0272-3

Cowley, S. W. H., & Lockwood, M. (1992). Excitation and decay of solar wind-driven flows in the magnetosphere-ionosphere system. *Annales Geophysicae*, *10*(1–2), 103–115.

Danilov, A. D. (2013). Ionospheric F-region response to geomagnetic disturbances. *Advances in Space Research*, *52*(3), 343–366. https://doi.org/10.1016/j.asr.2013.04.019

Darrouzet, F., De Keyser, J., Décréau, P. M. E., El Lemdani-Mazouz, F., & Vallières, X. (2008). Statistical analysis of plasmaspheric plumes with Cluster/WHISPER observations. *Annales Geophysicae*, *26*(8), 2403–2417. https://doi.org/10.5194/angeo-26-2403-2008

de la Beaujardiere, O., Lyons, L. R., & Friis-Christensen, E. (1991). Sondrestrom radar measurements of the reconnection electric field. *Journal of Geophysical Research*, *96*(A8), 13907–13912. https://doi.org/10.1029/91JA01174

Ellington, S. M., Moldwin, M. B., & Liemohn, M. W. (2016). Local time asymmetries and toroidal field line resonances: Global magnetospheric modeling in SWMF. *Journal of Geophysical Research: Space Physics*, *121*(3), 2033–2045. https://doi.org/10.1002/2015JA021920

Etemadi, A., Cowley, S. W. H., Lockwood, M., Bromage, B. J. I., Willis, D. M., & Lühr, H. (1988). The dependence of high-latitude dayside ionospheric flows on the North-South component of the IMF: A high time resolution correlation analysis using EISCAT "Polar" and AMPTE UKS and IRM data. *Planetary and Space Science*, *36*(5), 471–498. https://doi.org/10.1016/0032-0633(88)90107-9

Foster, J. C. (1993). Storm time plasma transport at middle and high latitudes. *Journal of Geophysical Research*, *98*(A2), 1675–1689. https://doi.org/10.1029/92JA02032

Foster, J. C., Coster, A. J., Erickson, P. J., Rich, F. J., & Sandel, B. R. (2004). Stormtime observations of the flux of plasmaspheric ions to the dayside cusp/magnetopause. *Geophysical Research Letters*, *31*(8). https://doi.org/10.1029/2004GL020082

Foster, J. C., Erickson, P. J., Coster, A. J., Goldstein, J., & Rich, F. J. (2002). Ionospheric signatures of plasmaspheric tails. *Geophysical Research Letters*, *29*(13), 1-1–1-4. https://doi.org/10.1029/2002GL015067

Foster, J. C., Erickson, P. J., Coster, A. J., Thaller, S., Tao, J., Wygant, J. R., & Bonnell, J. W. (2014). Storm time observations of plasmasphere erosion flux in the magnetosphere and ionosphere. *Geophysical Research Letters*, *41*(3), 762–768. https://doi.org/10.1002/2013GL059124

Foster, J. C., Erickson, P. J., Walsh, B. M., Wygant, J. R., Coster, A. J., & Zhang, Q. (2020). Multi-point observations of the geospace plume. In Q. Zong, P. Escoubet, D. Sibeck, G. Le, & H. Zhang (Eds.), *Geophysical monograph series* (1st ed., pp. 243–264). https://doi.org/10.1002/9781119509592.ch14

Foster, J. C., Rideout, W., Sandel, B., Forrester, W. T., & Rich, F. J. (2007). On the relationship of SAPS to storm-enhanced density. *Journal of Atmospheric and Solar-Terrestrial Physics*, *69*(3), 303–313. https://doi.org/10.1016/j.jastp.2006.07.021

Freeman, M. P., Chisham, G., & Coleman, I. J. (2007). Remote sensing of reconnection. In J. Birn, & E. Priest (Eds.), *Reconnection of magnetic fields* (Chap. 4.6, pp. 217–228). Cambridge University Press.

Fuselier, S. A., Burch, J. L., Cassak, P. A., Goldstein, J., Gomez, R. G., Goodrich, K., et al. (2016). Magnetospheric ion influence on magnetic reconnection at the duskside magnetopause. *Geophysical Research Letters*, *43*(4), 1435–1442. https://doi.org/10.1002/2015GL067358

Fuselier, S. A., Burch, J. L., Mukherjee, J., Genestreti, K. J., Vines, S. K., Gomez, R., et al. (2017). Magnetospheric ion influence at the dayside magnetopause. *Journal of Geophysical Research: Space Physics*, *122*(8), 8617–8631. https://doi.org/10.1002/2017JA024515

Hairston, M. R., & Heelis, R. A. (1995). Response time of the polar ionospheric convection pattern to changes in the north-south direction of the IMF. *Geophysical Research Letters*, *22*(5), 631–634. https://doi.org/10.1029/94GL03385

Halford, A. J., Fraser, B. J., & Morley, S. K. (2015). EMIC waves and plasmaspheric and plume density: CRRES results. *Journal of Geophysical Research: Space Physics*, *120*(3), 1974–1992. https://doi.org/10.1002/2014JA020338

Hubert, B., Milan, S. E., Grocott, A., Blockx, C., Cowley, S. W. H., & Gérard, J.-C. (2006). Dayside and nightside reconnection rates inferred from IMAGE FUV and Super Dual Auroral Radar Network data. *Journal of Geophysical Research*, *111*(A3). https://doi.org/10.1029/2005JA011140

Khan, H., & Cowley, S. (1999). Observations of the response time of high-latitude ionospheric convection to variations in the interplanetary magnetic field using EISCAT and IMP-8 data. *Annals of Geophysics*, *17*. https://doi.org/10.1007/s00585-999-1306-8

Lee, S. H., Zhang, H., Zong, Q.-G., Otto, A., Rème, H., & Liebert, E. (2016). A statistical study of plasmaspheric plumes and ionospheric outflows observed at the dayside magnetopause. *Journal of Geophysical Research: Space Physics*, *121*(1), 492–506. https://doi.org/10.1002/2015JA021540

Lee, S. H., Zhang, H., Zong, Q.-G., Otto, A., Sibeck, D. G., Wang, Y., et al. (2014). Plasma and energetic particle behaviors during asymmetric magnetic reconnection at the magnetopause. *Journal of Geophysical Research: Space Physics*, *119*(3), 1658–1672. https://doi.org/10.1002/2013JA019168

Lemaire, J. F. (2000). The formation plasmaspheric tails. *Physics and Chemistry of the Earth - Part C: Solar, Terrestrial & Planetary Science*, *25*(1), 9–17. https://doi.org/10.1016/S1464-1917(99)00026-4

Lockwood, M., & Cowley, S. W. H. (1999). Comment on "A statistical study of the ionospheric convection response to changing interplanetary magnetic field conditions using the assimilative mapping of ionospheric electrodynamics technique" by A.J. Ridley et al. *Journal of Geophysical Research*, *104*(A3), 4387–4391. https://doi.org/10.1029/1998JA900145

Lockwood, M., van Eyken, A. P., Bromage, B. J. I., Willis, D. M., & Cowley, S. W. H. (1986). Eastward propagation of a plasma convection enhancement following a southward turning of the interplanetary magnetic field. *Geophysical Research Letters*, *13*(1), 72–75. https://doi.org/10.1029/GL013i001p00072

Lopez, R. E. (2016). The integrated dayside merging rate is controlled primarily by the solar wind. *Journal of Geophysical Research: Space Physics*, *121*(5), 4435–4445. https://doi.org/10.1002/2016JA022556

Lopez, R. E., Bruntz, R., Mitchell, E. J., Wiltberger, M., Lyon, J. G., & Merkin, V. G. (2010). Role of magnetosheath force balance in regulating the dayside reconnection potential. *Journal of Geophysical Research*, *115*(A12). https://doi.org/10.1029/2009JA014597

Lopez, R. E., & Gonzalez, W. D. (2017). Magnetospheric balance of solar wind dynamic pressure. *Geophysical Research Letters*, *44*(7), 2991–2999. https://doi.org/10.1002/2017GL072817

Maruyama, N., Denton, M. H., Nishimura, Y., Henderson, M. G., Richards, P. G., Fedrizzi, M., et al. (2020). On the sources of cold and dense plasma in plasmasphere drainage plumes. *Space Physics*, *52*.

Maynard, N. C., & Chen, A. J. (1975). Isolated cold plasma regions: Observations and their relation to possible production mechanisms. *Journal of Geophysical Research*, *80*(7), 1009–1013. https://doi.org/10.1029/JA080i007p01009

McComas, D. J., Bame, S. J., Barraclough, B. L., Donart, J. R., Elphic, R. C., Gosling, J. T., et al. (1993). Magnetospheric plasma analyzer: Initial three-spacecraft observations from geosynchronous orbit. *Journal of Geophysical Research*, *98*, 13453–13465.

McFadden, J. P., Carlson, C. W., Larson, D., Bonnell, J., Mozer, F., Angelopoulos, V., et al. (2009). THEMIS ESA first science results and performance issues. In J. L. Burch, & V. Angelopoulos (Eds.), *The THEMIS mission* (pp. 477–508). https://doi.org/10.1007/978-0-387-89820-9_20

McFadden, J. P., Carlson, C. W., Larson, D., Ludlam, M., Abiad, R., Elliott, B., et al. (2009). The THEMIS ESA plasma instrument and in-flight calibration. In J. L. Burch, & V. Angelopoulos (Eds.), *he THEMIS mission* (pp. 277–302). https://doi.org/10.1007/978-0-387-89820-9_13

McWilliams, K. A., Yeoman, T. K., & Cowley, S. W. H. (2000). Two-dimensional electric field measurements in the ionospheric footprint of a flux transfer event. *Annales Geophysicae*, *18*(12), 1584–1598. https://doi.org/10.1007/s00585-001-1584-2

McWilliams, K. A., Yeoman, T. K., Sigwarth, J. B., Frank, L. A., & Brittnacher, M. (2001). The dayside ultraviolet aurora and convection responses to a southward turning of the interplanetary magnetic field. *Annales Geophysicae*, *19*(7), 707–721. https://doi.org/10.5194/angeo-19-707-2001

Mendillo, M. (2006). Storms in the ionosphere: Patterns and processes for total electron content. *Reviews of Geophysics*, *44*(4). https://doi.org/10.1029/2005RG000193

Mendillo, M., Papagiannis, M. D., & Klobuchar, J. A. (1972). Average behavior of the midlatitude F-region parameters NT, N max, and τ during geomagnetic storms. *Journal of Geophysical Research*, *77*(25), 4891–4895. https://doi.org/10.1029/JA077i025p04891

Moldwin, M. B., Zou, S., & Heine, T. (2016). The story of plumes: The development of a new conceptual framework for understanding magnetosphere and ionosphere coupling. *Annales Geophysicae*, *34*(12), 1243–1253. https://doi.org/10.5194/angeo-34-1243-2016

Nishida, A. (1966). Formation of plasmapause, or magnetospheric plasma knee, by the combined action of magnetospheric convection and plasma escape from the tail. *Journal of Geophysical Research*, *71*(23), 5669–5679. https://doi.org/10.1029/JZ071i023p05669

Ober, D. M., Horwitz, J. L., Thomsen, M. F., Elphic, R. C., McComas, D. J., Belian, R. D., & Moldwin, M. B. (1997). Premidnight plasmaspheric "plumes". *Journal of Geophysical Research*, *102*(A6), 11325–11334. https://doi.org/10.1029/97JA00562

Ouellette, J. E., Lyon, J. G., Brambles, O. J., Zhang, B., & Lotko, W. (2016). The effects of plasmaspheric plumes on dayside reconnection. *Journal of Geophysical Research: Space Physics*, *121*(5), 4111–4118. https://doi.org/10.1002/2016JA022597

Papagiannis, M. D., Mendillo, M., & Klobuchar, J. A. (1971). Simultaneous storm-time increases of the ionospheric total electron content and the geomagnetic field in the dusk sector. *Planetary and Space Science*, *19*(5), 503–511. https://doi.org/10.1016/0032-0633(71)90166-8

Pinnock, M., Chisham, G., Coleman, I. J., Freeman, M. P., Hairston, M., & Villain, J.-P. (2003). The location and rate of dayside reconnection during an interval of southward interplanetary magnetic field. *Annales Geophysicae*, *21*(7), 1467–1482. https://doi.org/10.5194/angeo-21-1467-2003

Pinnock, M., Rodger, A. S., Baker, K. B., Lu, G., & Hairston, M. (1999). Conjugate observations of the day-side reconnection electric field: A GEM boundary layer campaign. *Annales Geophysicae*, *17*(4), 443–454. https://doi.org/10.1007/s00585-999-0443-4

Prölss, G. W. (1995). Ionospheric F-region storms. In H. Volland (Ed.), *Handbook of atmospheric electrodynamics* (Vol. 2, pp. 195–248). CRC Press.

Richmond, A. D., & Lu, G. (2000). Upper-atmospheric effects of magnetic storms: A brief tutorial. *Journal of Atmospheric and Solar-Terrestrial Physics*, *62*(12), 1115–1127. https://doi.org/10.1016/S1364-6826(00)00094-8

Rideout, W., & Coster, A. (2006). Automated GPS processing for global total electron content data. *GPS Solutions*, *10*(3), 219–228. https://doi.org/10.1007/s10291-006-0029-5

Ruohoniemi, J. M., & Baker, K. B. (1998). Large-scale imaging of high-latitude convection with Super Dual Auroral Radar Network HF radar observations. *Journal of Geophysical Research*, *103*(A9), 20797–20811. https://doi.org/10.1029/98JA01288

Ruohoniemi, J. M., & Greenwald, R. A. (1998). The response of high-latitude convection to a sudden southward IMF turning. *Geophysical Research Letters*, *25*(15), 2913–2916.

Saunders, M. A., Freeman, M. P., Southwood, D. J., Cowley, S. W. H., Lockwood, M., Samson, J. C., et al. (1992). Dayside ionospheric convection changes in response to long-period interplanetary magnetic field oscillations: Determination of the ionospheric phase velocity. *Journal of Geophysical Research*, *97*(A12), 19373–19380. https://doi.org/10.1029/92JA01383

Sheeley, B. W., Moldwin, M. B., Rassoul, H. K., & Anderson, R. R. (2001). An empirical plasmasphere and trough density model: CRRES observations. *Journal of Geophysical Research*, *106*(A11), 25631–25641. https://doi.org/10.1029/2000JA000286

Southwood, D. J. (1985). Theoretical aspects of ionosphere-magnetosphere-solar wind coupling. *Advances in Space Research*, *5*(4), 7–14. https://doi.org/10.1016/0273-1177(85)90110-3

Spasojevic, M., & Fuselier, S. A. (2009). Temporal evolution of proton precipitation associated with the plasmaspheric plume. *Journal of Geophysical Research*, *114*(A12). https://doi.org/10.1029/2009JA014530

Summers, D., Ni, B., Meredith, N. P., Horne, R. B., Thorne, R. M., Moldwin, M. B., & Anderson, R. R. (2008). Electron scattering by whistler-mode ELF hiss in plasmaspheric plumes. *Journal of Geophysical Research*, *113*(A4). https://doi.org/10.1029/2007JA012678

Su, Y.-J., Borovsky, J. E., Thomsen, M. F., Elphic, R. C., & McComas, D. J. (2000). Plasmaspheric material at the reconnecting magnetopause. *Journal of Geophysical Research*, *105*(A4), 7591–7600. https://doi.org/10.1029/1999JA000266

Thomsen, M. F., Noveroske, E., Borovsky, J. E., & McComas, D. J. (1999). *Calculation of moments from measurements by the Los Alamos magnetospheric plasma analyzer* (LA Rep. LA-13566-MS). Los Alamos National Laboratory.

Todd, H., Cowley, S. W. H., Lockwood, M., Willis, D. M., & Lühr, H. (1988). Response time of the high-latitude dayside ionosphere to sudden changes in the north-south component of the IMF. *Planetary and Space Science*, *36*(12), 1415–1428. https://doi.org/10.1016/0032-0633(88)90008-6

Walsh, B. M., Foster, J. C., Erickson, P. J., & Sibeck, D. G. (2014). Simultaneous Ground- and Space-Based Observations of the Plasmaspheric Plume and Reconnection. *Science*, *343*(6175), 1122–1125. https://doi.org/10.1126/science.1247212

Walsh, B. M., Phan, T. D., Sibeck, D. G., & Souza, V. M. (2014). The plasmaspheric plume and magnetopause reconnection. *Geophysical Research Letters*, *41*(2), 223–228. https://doi.org/10.1002/2013GL058802

Walsh, B. M., Sibeck, D. G., Nishimura, Y., & Angelopoulos, V. (2013). Statistical analysis of the plasmaspheric plume at the magnetopause. *Journal of Geophysical Research: Space Physics*, *118*(8), 4844–4851. https://doi.org/10.1002/jgra.50458

Wang, S., Kistler, L. M., Mouikis, C. G., & Petrinec, S. M. (2015). Dependence of the dayside magnetopause reconnection rate on local conditions. *Journal of Geophysical Research: Space Physics*, *120*(8), 6386–6408. https://doi.org/10.1002/2015JA021524

Yizengaw, E., Moldwin, M. B., & Galvan, D. A. (2006). Ionospheric signatures of a plasmaspheric plume over Europe. *Geophysical Research Letters*, *33*(17). https://doi.org/10.1029/2006GL026597

Yuan, Z., Li, M., Xiong, Y., Li, H., Zhou, M., Wang, D., et al. (2013). Simultaneous observations of precipitating radiation belt electrons and ring current ions associated with the plasmaspheric plume. *Journal of Geophysical Research: Space Physics*, *118*(7), 4391–4399. https://doi.org/10.1002/jgra.50432

Yuan, Z., Zhao, L., Xiong, Y., Deng, X., & Wang, J. (2011). Energetic particle precipitation and the influence on the sub-ionosphere in the SED plume during a super geomagnetic storm. *Journal of Geophysical Research*, *116*, A09317. https://doi.org/10.1029/2011JA016821

Zhang, B., Brambles, O. J., Cassak, P. A., Ouellette, J. E., Wiltberger, M., Lotko, W., & Lyon, J. G. (2017). Transition from global to local control of dayside reconnection from ionospheric-sourced mass loading. *Journal of Geophysical Research: Space Physics*, *122*(9), 9474–9488. https://doi.org/10.1002/2016JA023646

Zhang, B., Brambles, O. J., Wiltberger, M., Lotko, W., Ouellette, J. E., & Lyon, J. G. (2016). How does mass loading impact local versus global control on dayside reconnection? Mass loading and dayside reconnection. *Geophysical Research Letters*, *43*(5), 1837–1844. https://doi.org/10.1002/2016GL068005

Zou, Y., Walsh, B. M., Nishimura, Y., Angelopoulos, V., Ruohoniemi, J. M., McWilliams, K. A., & Nishitani, N. (2019). Local time extent of magnetopause reconnection using space–ground coordination. *Annales Geophysicae*, *37*(2), 215–234. https://doi.org/10.5194/angeo-37-215-2019